DAO Office Note 96-07

Office Note Series on Global Modeling and Data Assimilation

A Study on Assimilating Potential Vorticity Data

Yong Li[*]
Richard Menard[†]
Lars Peter Riishøjgaard[†]
Stephen E. Cohn
Richard B. Rood

Data Assimilation Office, Goddard Laboratory for Atmospheres
Goddard Space Flight Center, Greenbelt, Maryland
[*] *General Sciences Corporation*
[†] *University Space Research Association*

Abstract

The high correlation between the potential vorticity (PV) and the distribution of some chemical tracers (e.g., O_3) points to the possibility of using tracer observations as proxy PV data. Especially in the stratosphere, there are plentiful tracer observations but a general lack of reliable wind observations, and the correlation is most remarkable.

The issue investigated in this study is how model dynamics would respond to inserted PV data. Numerical experiments of identical twin type have been conducted with a simple nudging algorithm and a global shallow water model based on PV and divergence (PV-D model). Successes in reconstructing the full model fields have been obtained when only PV data are inserted if an appropriate value for the nudging coefficient is used. Relative advantages have been demonstrated as compared with the results when only geopotential data are inserted. The longest waves were found to be subject to spurious growth when the model PV is forced too strongly toward the PV data. But with the use of additional geopotential data, which actually represents the case in real data assimilation practice (we usually have temperature data), such spurious growth is shown to be alleviated. Adding a penalty term to the divergence equation is also a viable way to control such spurious growth. Linear analysis agrees with the numerical experiments and gives insightful understanding.

This study sheds promising light on assimilating PV data and thus points our attention to the potential power that tracer observations, as proxy PV data, may offer in a data assimilation system.

Contents

List of Figures

1 Introduction

In the stratosphere, there is a general lack of reliable wind observations. Aside from some radiosonde reporting in the lower stratosphere, the only source of global stratospheric wind measurements at present, originates from the High Resolution Doppler Imager (HRDI) on board the Upper Atmosphere Research Satellite (UARS). However, these data have been little used because they are daylight-only retrievals, have large observational biases and, showed little to modest impact in stratospheric assimilations (Richard Swinbank, personal communication). Traditionally, it has been attempted to obtain wind observations indirectly. Charney et al. (1969) showed that the wind field could be recovered through a model with temperature being periodically replaced by observations. Preliminary successes were documented in their idealized experiments, but problems such as undesired gravity waves due to data insertion were encountered. Today satellite temperatures are being assimilated and gravity waves removed by proper filtering or initialization. Nevertheless, wind information remain indirect with wind analysis increments being essentially geostrophic. For the future, space-based lidars have been proposed for stratospheric wind measurements. But they are technologically difficult, expensive and funding appears uncertain. Alternative technologies such as the Stratospheric Winds Imager Payload Experiment (SWIPE), is being under development and will require some time to become operational.

Another source of wind information comes from the measurements of chemical constituents. Many of such constituents (e.g., O_3, CH_4, and N_2O) can be used as tracers since they have long life-spans. Recently, such efforts have been made by using transport models. For example, Daley (1995) studied a one-dimensional extended Kalman filter problem and Riishøjgaard (1996) studied a two-dimensional global problem in the context of variational methods. The approach of using transport models to retrieve wind information, regardless of the assimilation algorithms, shares one common shortcoming, i.e., constituent observations do not contain any information of the wind components tangential to the isopleths of the constituent distribution. Therefore, we cannot expect such a method to yield significant improvements on the wind analysis except in those regions where sharp gradients are coupled with strong cross-contour flows.

It has been noticed that the PV field and the ozone field are highly correlated, particularly in the stratosphere. Early observational evidence was presented by Danielsen (1968) and was further confirmed and examined by Danielsen et al. (1987). Recent studies which suggest, examine or make use of such correlations include Lait et al. (1990), Douglass et al. (1990), Lary et al. (1995), Allaart et al. (1993; henceforth A93), and Riishøjgaard and Källén (1996). So there is such a possibility of using the tracer information as proxy PV data.

We have known for some time that PV is a dynamically significant quantity (see e.g., Hoskins et al. 1985 for a review). We may even derive both the wind field and the mass field from a global distribution of PV if certain balance conditions are assumed. Recently, Vallis (1996) proposed a variety of models either based on the shallow water equations or on the stratified primitive equations. Different balance conditions were proposed in an attempt to describe different types of flow. Certain degree of success was demonstrated

in the numerical experiments that other dynamical quantities are retrieved using the PV inversion approaches. But the limitations imposed by the balance conditions are obvious. It was indeed noticed in Vallis (1996) that the reconstruction of the divergence is, in most situations, very unsatisfactory. In some situations, it is hardly recovered at all.

We can expect improvements if the balance conditions are avoided, such as in the case of primitive equation models. But a PV field contains information of both the wind field and the mass field. There are nonunique combinations of these two fields which would yield the same PV if no balance condition is assumed. The dynamical adjustments between the wind field and the mass field are to be accomplished inherently by the model. But how would a primitive equation model respond to externally inserted PV? This is the main theme of this study.

People use various indicators to measure the quality and efficiency of a data assimilation system. The following three are commonly considered: (1) the asymptotic error level which measures the ultimate difference between the observation and the analysis; (2) the rate of convergence or the speed at which the asymptotic error is reached; (3) the level of spurious excitation of gravity waves due to the assimilation process. For this third reason, Daley and Puri (1980) argued that it is desirable to have an assimilation system in which the inserted data do not drive the model too far off the slow manifold.

We use a global shallow water model which is based on the advection of PV (referred to as PV-D model hereafter) developed by Bates *et al.* (1995; henceforth BLBMR) and extended to include orography by Li and Bates (1996; henceforth LB96). A simple nudging method is adopted here for the data insertion.

The paper is planned as follows. In Section 2, we briefly describe the PV-D model and the data insertion algorithm. In Section 3, we describe the design of the numerical experiments followed by some discussions on the results. Linear analyses are presented in Section 4. In Section 5, we present some results of assimilating TOMS total ozone data. Finally in Section 6, we offer concluding remarks and discussions.

2   The Shallow Water PV-D Model and The Data Insertion Algorithm

2.1   The PV-D model

We present a brief description of the model here, for detailed description of the shallow water PV-D model can be found in BLBMR and LB96.

The model equations consist of the PV, divergence and continuity equations. The continuous form of the PV equation is

$$\frac{d}{dt}\left(\frac{\nabla^2\psi + f}{\Phi}\right) = 0 \tag{1}$$

2

where ψ is the streamfunction and f the Coriolis force. After SLSI discretization, this equation becomes

$$\left(\frac{\nabla^2\psi + f}{\Phi}\right)^{n+1} + \frac{\beta\tau_1'}{\Phi_*^n}\left[\frac{1}{a\cos\phi}\frac{\partial\psi}{\partial\lambda} + \frac{1}{a}\frac{\partial\chi}{\partial\phi}\right]^{n+1} = r_1 \tag{2}$$

where χ is the velocity potential, β the latitudinal variation of f, r_1 the forcing term (LB96), $\tau_1' = \frac{\Delta t}{2}$ with Δt denoting the time stepsize, and $(\ )_*$ denotes a departure-point value. The term associated with β comes from a centered implicit discretization of the β-term after the Taylor expansion of f_*. Such a treatment is to alleviate the numerical instability of Rossby waves (BLBMR).

The SLSI discretized divergence equation is obtained through first SLSI discretizing the horizontal momentum equation in its vector form and then taking a divergence operator, which gives

$$\left(\nabla^2\chi + \tau_1\left[\nabla^2\Phi - f\nabla^2\psi + \beta\left(\frac{1}{a\cos\phi}\frac{\partial\chi}{\partial\lambda} - \frac{1}{a}\frac{\partial\psi}{\partial\phi}\right)\right]\right)^{n+1} = r_2 - \tau_1\nabla^2\Phi_s \tag{3}$$

where $\tau_1 = \frac{1+\varepsilon}{2}\Delta t$ with ε being the first-order uncentering parameter (chosen to be zero in this study), Φ the geopotential depth, Φ_s the geopotential height of surface orography, and r_2 the forcing term defined as in LB96.

For the continuity equation,

$$\frac{d\Phi}{dt} = -\Phi\nabla^2\chi, \tag{4}$$

the SLSI discretization is straightforward, which is

$$\Phi^{n+1}\left(1 + \tau_1\nabla^2\chi\right)^{n+1} = r_3. \tag{5}$$

The discretized model equations (2), (3) and (5) are solved with the nonlinear multigrid technique (Ruge *et al.* 1996). This model, with an independent equation for PV, conveniently facilitates our study on PV data insertion.

2.2 The data insertion algorithm

The data insertion algorithm is the simple nudging technique which has been studied extensively (e.g., Davies and Turner 1977; Kuo *et al.* 1993) since its early use (Anthes 1974). This is to force certain model fields toward the corresponding available data fields through linear terms that characterize the model-data misfit. Despite its simplicity, the algorithm is a good tool for a proof-of-concept type of study presented here.

When we insert PV data, the only equation that we modify is the PV equation. But when we insert the geopotential data, we need to modify both the continuity equation and the PV equation. Now the PV and continuity equations, written in their continuous forms, are as follows:

$$\frac{d}{dt}\left(\frac{\nabla^2\psi + f}{\Phi}\right) = \alpha_{pv}\left(PV_{data} - PV\right) - \alpha_\Phi\left(\frac{PV}{\Phi}\right)\left(\Phi_{data} - \Phi\right) \tag{6}$$

3

$$\frac{d\Phi}{dt} = -\Phi\nabla^2\chi + \alpha_\Phi \left(\Phi_{data} - \Phi\right) \tag{7}$$

where

$$\alpha_{pv} = \frac{1}{T_{pv}}; \quad and \quad \alpha_\Phi = \frac{1}{T_\Phi}.$$

with T_{pv} and T_Φ denoting the e-folding times for the nudging.

A penalty term is added to the divergence equation after observing in the numerical experiments that the divergence leads in the spurious growth of longest waves when PV data are inserted with a large nudging coefficient. The SLSI discretized divergence equation then becomes:

$$\left(\nabla^2\chi + \tau_1 \left[\nabla^2\Phi - f\nabla^2\psi + \beta\left(\frac{1}{a\cos\phi}\frac{\partial\chi}{\partial\lambda} - \frac{1}{a}\frac{\partial\psi}{\partial\phi}\right)\right]\right)^{n+1} = r_2 - \tau_1\nabla^2\Phi_s - \mu_D\Delta t\left(\nabla^2\chi\right)^n \tag{8}$$

where $\mu_D = \frac{1}{T_{div}}$ is the divergence penalty coefficient with a time-scale T_{div}.

3 Numerical Experiments

3.1 Experiment design

Experiments of identical-twin type are carried out in this study, in which one model integration, the control, is regarded as the "data". These data are then inserted into the model integrations which start from different initial conditions. We refer to these integrations as "assimilation runs".

A polar vortex erosion case, similar to that used by Bates and Li (1996) for a comparison study of numerical simulations, is used in this study again. Despite its simplicity, such a simulation captures many basic features (e.g., Rossby wave breaking) of a major flow pattern for the winter polar stratosphere. Since Juckes and McIntyre (1987), many have conducted model simulations using various derivatives of this case for dynamical investigations (e.g., Mariotti et al. 1994; Norton 1994; Polvani et al. 1995).

For the control, the model is initialized with a horizontal zonal flow displayed in Figure 1. The initial geopotential is derived from the gradient wind balance. The model is then integrated for 50 days with the following orographic forcing:

$$h\left(\lambda, \phi, t\right) = -H_s A\left(t\right) B\left(\phi\right) sin\left(\lambda\right) \tag{9}$$

with h denoting the height of the orography. We choose $H_s = 0.72$ km and assign $A\left(t\right)$ and $B\left(\phi\right)$ the form shown in Fig.2(a) and (b). The evolution of the PV field is displayed in Figures 3(a)-(d).

For the "assimilation runs", the model starts from Day 20 but initialized with the model fields of Day 10 of the control. This implies that the model initial condition bears an error of a magnitude characterized by two states with a 10-day phase shift. Data are inserted

at every grid-point and every time step. In all the experiments a horizontal resolution of 128x65 points on a regular latitude/longitude grid and a timestep of 30 minutes are used.

3.2 PV data insertion

In this section, we present results of inserting PV data only. Figure 4(a) displays the RMS error of the PV field for various e-folding times. "Model" implies that no data are inserted and is presented here as a reference. All the "assimilation runs" show an initial decrease of the RMS error. The shorter the e-folding time, the faster the decreasing rate. With T_{pv} = 24, 48 or 96 hours, the RMS errors for all quantities decrease monotonically. But for T_{pv} = 6 hours and T_{pv} = 12 hours, they start to increase at later times. It may be most interesting to examine the divergence field (Figure 4(b)). We see that the RMS errors increase from the beginning of data insertion for T_{pv} = 6 hours and T_{pv} = 12 hours. The RMS error of geopotential height starts to increase at a time later than the divergence but earlier than PV (as in Figure 4(c)).

We now examine more closely two "runs", a good one (T_{pv} = 48 hours) and a bad one (T_{pv} = 6 hours). Figure 5(a)-(c) display the divergence fields at Day 30 for the control, the assimilated with T_{pv} = 48 and that with T_{pv}6 hours respectively. The assimilation with T_{pv} = 48 (Figure 5 (b)) presents a success—the assimilated divergence is almost identical to the control. Figure 6 displays the RMS errors of PV, geopotential, divergence and vorticity of this run normalized by their respective initial values. The errors of PV, geopotential and vorticity decrease at the same rate, and that of the divergence follows the trend closely. For T_{pv} = 6 hours, the assimilated divergence (Figure 5 (c)) deviates dramatically from the control. There is evidently strong spurious growth of the longest waves.

3.3 Geopotential data insertion

By examining geopotential data insertion in comparison with the PV data insertion, we wish to learn whether assimilating PV data actually gives us any advantage or it is merely redundant.

An experiment of direct insertion, i.e., the model geopotential being replaced immediately by the "data" every time step, is also conducted. This is what Charney *et al.* (1969) investigated. Figures 6(a)-(c) display the RMS errors of the assimilated PV, divergence and geopotential height. Figure 7 shows the normalized RMS errors of PV, geopotential, vorticity and divergence for the case of direct insertion, and Figure 8 is the same as Figure 7 but for the case of T_ϕ = 48 hours. A few things can be noted from these results: 1) The errors decrease more slowly than in the case of PV data insertion. This is recognizable in all fields with the divergence being most marked. It suggests that PV "drives" the system more strongly than the geopotential; 2) Geopotential data insertion tends to excite spurious gravity-inertia waves. Figure 10(a)-(b) display the divergence fields of Days 24 and 50 for the case of direct insertion. The spurious gravity waves are very obvious at Day 24. They remain strong for quite some time and are still evident by Day 50. These spurious waves

are, however, absent in all the PV insertion runs; 3) With $T = 48$ hours, geopotential data insertion does not lead to significant decrease of the RMS errors while PV data insertion gives optimal results; 4) With strong nudging, geopotential data insertion does not lead to the spurious growth of longest waves, but PV data insertion may.

3.4 Mixed data insertion

In reality, we usually have as much, if not more, temperature information as proxy PV data. It is interesting to examine the case when we insert both geopotential and PV data. We intend to assess through these experiments whether the spurious growth associated with the longest waves would be alleviated when an additional constraint on the mass field is imposed by the use of geopotential data.

We repeat the experiment of PV data insertion with $T_{pv} = 6$ hours but now also with geopotential data insertion with $T_\phi = 6$, 12 and 24 hours. The assimilated divergence fields at Day 30 are presented in Figure 11(a)-(c). The longest waves are, indeed, stabilized. No spurious growth is now detected. Additional numerical experiments (results not presented) show that the instability reappears when T_ϕ increases to 48 hours. The critical T_ϕ is proportional to T_{pv}. In a realistic data assimilation system, T_{pv} is not likely to be larger than T_ϕ considering the data availability and quality. So the spurious growth of the longest waves is expected not to be a problem in practice.

3.5 PV data insertion with divergence penalty

As we have seen, divergence always takes the lead in the cases with spurious growth associated with the longest waves. This motivates us to examine the possibility of including a divergence penalty term in the divergence equation. And we repeat the PV data insertion experiment with $T_{pv} = 6$ hours. In Figure 12(a)-(c), we display the divergence field at Day 30 for $T_{div} = 6$, 12 and 24 hours. Indeed, the spurious long wave instability is now suppressed. Again, more numerical experiments (results not presented) show that the long wave instability reappears when T_{div} increases up to 48 hours. And the critical T_{div} is proportional to the T_{pv} being used.

4 Linear Analysis

The numerical results we have seen so far point our attention to the potential power of assimilating PV data. We now conduct linear analyses in order to better understand these results. Linearized shallow water equations can be written as:

$$\frac{\partial \zeta'}{\partial t} + f\delta' + \beta v' = 0 \tag{10}$$

$$\gamma \frac{\partial \delta'}{\partial t} + \left(\nabla^2 \Phi' - f\zeta' + \beta u' \right) = 0 \tag{11}$$

$$\frac{\partial \Phi'}{\partial t} + \bar{\bar{\Phi}} \delta' = 0 \tag{12}$$

where ζ' is the vorticity perturbation, δ' the divergence perturbation, Φ' the geopotential perturbation, u' and v' the horizontal velocity perturbations, $\bar{\bar{\Phi}}$ the geopotential height of the basic state. The parameter γ is used to choose between a primitive equation system ($\gamma = 1$) and a balance equation system ($\gamma = 0$).

4.1   Free oscillations

Consider a one-dimensional problem in which there is no variation in the y-direction:

$$\frac{\partial}{\partial t} \left(\frac{1}{\bar{\bar{\Phi}}} \frac{\partial v'}{\partial x} - \frac{f}{\bar{\bar{\Phi}}^2} \Phi' \right) + \frac{\beta}{\bar{\bar{\Phi}}} v' = 0 \tag{13}$$

$$\gamma \frac{\partial}{\partial t} \left(\frac{\partial u'}{\partial x} \right) + \left(\frac{\partial^2 \Phi'}{\partial x^2} - f \frac{\partial v'}{\partial x} + \beta u' \right) = 0 \tag{14}$$

$$\frac{\partial \Phi'}{\partial t} + \bar{\bar{\Phi}} \frac{\partial u'}{\partial x} = 0. \tag{15}$$

Assuming that the solutions to the above system take the following form:

$$\begin{pmatrix} u' \\ v' \\ \Phi' \end{pmatrix} = \begin{pmatrix} \hat{u} \\ \hat{v} \\ \hat{\Phi} \end{pmatrix} e^{i(kx+\omega t)}, \tag{16}$$

we can then obtain

$$\left(\frac{\beta - k\omega}{\bar{\bar{\Phi}}} \right) \hat{v} - i \left(\frac{\omega f}{\bar{\bar{\Phi}}^2} \right) \hat{\Phi} = 0 \tag{17}$$

$$(\beta - \gamma k\omega) \hat{u} - i (kf) \hat{v} - k^2 \hat{\Phi} = 0 \tag{18}$$

$$\omega \hat{\Phi} + (k\bar{\bar{\Phi}}) \hat{u} = 0. \tag{19}$$

These lead to the dispersion equation:

7

$$\gamma\omega^3 - (1+\gamma)\,\omega_R\omega^2 - \left(\omega_G^2 + \omega_I^2 - \omega_R^2\right)\omega + \left(\omega_G^2\omega_R\right) = 0 \tag{20}$$

where $\omega_G = \sqrt{k^2\bar{\Phi}}$, $\omega_I = f$ and $\omega_R = \frac{\beta}{k}$ are, respectively, frequencies of pure gravity waves, inertia waves and Rossby waves. We express all the solutions in terms of $\hat{\Phi}$:

$$\hat{u} = -\left(\frac{\omega}{k\bar{\Phi}}\right)\hat{\Phi}; \quad \hat{v} = i\left[\frac{\omega f}{\bar{\Phi}\,(\beta - k\omega)}\right]\hat{\Phi} \tag{21}$$

$$\hat{\zeta} = -\left[k\frac{\omega f}{\bar{\Phi}\,(\beta - k\omega)}\right]\hat{\Phi}; \quad \hat{\delta} = -i\left(\frac{\omega}{\bar{\Phi}}\right)\hat{\Phi} \tag{22}$$

including the potential vorticity which is:

$$\hat{PV'} = -\left[\frac{\beta f}{\bar{\Phi}^2\,(\beta - k\omega)}\right]\hat{\Phi}. \tag{23}$$

4.2 Forced solution with data insertion

The linear equations, which include the forcing terms for the data insertion as well as the divergence penalty, are:

$$\frac{\partial}{\partial t}\left(\frac{1}{\bar{\Phi}}\frac{\partial v'}{\partial x} - \frac{f}{\bar{\Phi}^2}\Phi'\right) + \frac{\beta}{\bar{\Phi}}v' = \alpha_{pv}\left[PV'_{data} - PV'\right] - \alpha_\phi\frac{f}{\bar{\Phi}^2}\left(\Phi'_{data} - \Phi'\right) \tag{24}$$

$$\gamma\frac{\partial}{\partial t}\left(\frac{\partial u'}{\partial x}\right) + \left(\frac{\partial^2\Phi'}{\partial x^2} - f\frac{\partial v'}{\partial x} + \beta u'\right) = -\mu_D\left(\frac{\partial u'}{\partial x}\right) \tag{25}$$

$$\frac{\partial\Phi'}{\partial t} + \bar{\Phi}\frac{\partial u'}{\partial x} = -\alpha_\phi\left(\Phi'_{data} - \Phi'\right) \tag{26}$$

Assume a case of perfect observation in which the data are a set of free modes described by (21)-(23), i.e.,

$$(PV')_{data} = -\frac{\beta f}{\bar{\Phi}^2\,(\beta - k\omega)}\hat{\Phi}_{data}e^{i(kx+\omega t)}, \tag{27}$$

$$(\Phi')_{data} = \hat{\Phi}_{data}e^{i(kx+\omega t)}. \tag{28}$$

We intend to examine how the solutions approach the inserted data. Substitution of (27) and (28) into (24)-(26) gives us the following:

8

$$\left[\frac{ik}{\bar{\Phi}}\frac{d}{dt} + \frac{\beta - k\omega}{\bar{\Phi}} + i\frac{\alpha_{pv}k}{\bar{\Phi}}\right]\hat{v}\left(t\right) \;+\; \left[-\frac{f}{\bar{\Phi}^2}\frac{d}{dt} - i\frac{\omega f}{\bar{\Phi}^2} - \frac{\alpha_{pv}f}{\bar{\Phi}^2}\right]\hat{\Phi}\left(t\right)$$

$$= \; -\frac{f}{\bar{\Phi}^2}\left[\frac{\left(\alpha_{pv} + \alpha_\phi\right)\beta - \alpha_\phi k\omega}{\beta - k\omega}\right]\hat{\Phi}_{data} \tag{29}$$

$$\left[i\gamma k\frac{d}{dt} + \beta - \gamma k\omega + ik\mu_D\right]\hat{u}\left(t\right) - i\left(kf\right)\hat{v}\left(t\right) - k^2\hat{\Phi}\left(t\right) = 0 \tag{30}$$

$$\left(\frac{d}{dt} + \alpha_\phi + i\omega\right)\hat{\Phi}\left(t\right) + i\left(k\bar{\Phi}\right)\hat{u}\left(t\right) = \alpha_\phi\hat{\Phi}_{data} \tag{31}$$

From (29)–(31), we can obtain

$$A\frac{d^3 X_\phi\left(t\right)}{dt^3} + B\frac{d^2 X_\phi\left(t\right)}{dt^2} + C\frac{dX_\phi\left(t\right)}{dt} + DX_\phi\left(t\right) = E \tag{32}$$

where $X_\phi\left(t\right) = \hat{\Phi}\left(t\right)/\hat{\Phi}_{data}$ denotes the ratio of the amplitude of linear solution for the geopotential to that of the data, and

$$
\begin{aligned}
A \;=\;& \gamma \\
B \;=\;& \left[\gamma\left(\alpha_{pv} + \alpha_\phi\right) + \mu_D\right] + i\left[-\left(1 + \gamma\right)\omega_R + 3\gamma\omega\right] \\
C \;=\;& \left[\omega_G^2 + \omega_I^2 - \omega_R^2 - 3\gamma\omega^2 + 2\left(1 + \gamma\right)\omega_R\omega + \mu_D\left(\alpha_{pv} + \alpha_\phi\right) + \gamma\alpha_{pv}\alpha_\phi\right] \\
& + i\left[2\left(\mu_D + \gamma\left(\alpha_{pv} + \alpha_\phi\right)\right)\omega - \left(\mu_D + \alpha_{pv} + \left(1 + \gamma\right)\alpha_\phi\right)\omega_R\right] \\
D \;=\;& \left[\alpha_{pv}\omega_G^2 + \left(\alpha_{pv} + \alpha_\phi\right)\omega_I^2 - \alpha_\phi\left(\omega_R - \omega\right)\left(\omega_R - \gamma\omega\right)\right. \\
& \left. + \mu_D\omega\left(\omega_R - \omega\right) + \alpha_{pv}\omega\left(\omega_R - \gamma\omega\right) + \alpha_{pv}\alpha_\phi\mu_D\right] \\
& + i\left[-\omega_G^2\left(\omega_R - \omega\right) + \omega_I^2\omega - \omega\left(\omega_R - \omega\right)\left(\omega_R - \gamma\omega\right)\right. \\
& \left. - \mu_D\alpha_\phi\left(\omega_R - \omega\right) - \alpha_{pv}\alpha_\phi\left(\omega_R - \gamma\omega\right) + \alpha_{pv}\mu_D\omega\right] \\
E \;=\;& \alpha_{pv}\left(\frac{\omega_R\omega_I^2}{\omega_R - \omega}\right) + \alpha_\phi\left[\omega_I^2 - \left(\omega_R - \omega\right)\left(\omega_R - \gamma\omega\right) + \alpha_{pv}\mu_D\right] \\
& + i\alpha_\phi\left[-\mu_D\left(\omega_R - \omega\right) - \alpha_{pv}\left(\omega_R - \gamma\omega\right)\right].
\end{aligned}
$$

For a given wave length, we solve (20) and choose the ω that represents the slow mode. Parameters A, B, C, D and E can then be determined and $X_\phi\left(t\right)$ is solved through (32). The quantity $|X_\phi\left(t\right)|$ is then examined for wavenumbers 1 through 5 (measured along a zonal circle) with f and β defined at 45^0N and $\bar{\Phi} = 10$km. The initial amplitudes are chosen to be zero for all wavenumbers. We focus our discussion on the results obtained for the primitive equations ($\gamma = 1$) since the balance equation ($\gamma = 0$) has been found to give essentially the same results.

4.2.1 Analysis of PV data insertion

We first examine a case in which only PV data are inserted with $\alpha_{pv} = \frac{1}{T_{pv}}$, and both α_ϕ and μ_D are zero, i.e., no geopotential data and no divergence penalty.

In Figures 13(a)-(b), we display $|X_\phi|$ for $T_{pv} = 6$ hours and $T_{pv} = 48$ hours respectively. For $T_{pv} = 6$ hours, the shorter waves are being recovered quickly and the long waves (wavenumbers one, two and three) exhibit a tendency of spurious growth, with wavenumber one being most marked. As T_{pv} increases, the long waves tend to be stabilized. For $T_{pv} = 48$ hours, only wavenumber one is weakly growing. The decreasing instability with increasing T_{pv} for the long waves, is consistent with the numerical results. But the linear analysis seems to over-estimate such instability. This discrepancy may be due to the actual model being nonlinear.

Another feature that deserves our notice is that different scales converge to the data at the same rate. We may argue, based on this, that PV data insertion leads to a recovery for the smaller scales as efficiently as for the large scales.

4.2.2 Analysis of geopotential data insertion

In this section, we discuss the case where only geopotential data are inserted with $\alpha_\phi = \frac{1}{T_\phi}$, and both α_{pv} and μ_D are zero. In Figures 14 (a)-(c), we display $|X_\phi|$ for the cases of $T_\phi = 1$, 6 and 48 hours respectively. A few features can be noticed as we compare with the PV data insertion analysis:

1) Regardless of the length of T_ϕ, the instability associated with the long waves is absent, unlike in the case of PV data insertion;

2) In general, geopotential data insertion yields slower convergence than PV data insertion (Compare between Figure 14 (b) and Figure 13 (a), as well as between Figure 14 (c) and Figure 13 (b)). With $T_\phi = 48$ hours, for example, PV data insertion gives very good results but geopotential data insertion yields minimal recovery.

3) There is strong scale-dependency of convergence for the case of geopotential data insertion, with the small scales being recovered much more slowly. But the PV data insertion does not show such scale-dependency of convergence.

We may attribute some of the above advantageous results to the fact that PV data insertion imposes information of both the mass field and the wind field but geopotential data insertion imposes only the latter. Williamson and Kasahara (1971) argued that wind adjusts to temperature updating better for large scales while temperature adjusts to wind updating better for smaller scales. Kistler and McPherson (1975) found that by just using the wind calculated from the geopotential with local geostrophic balance, the convergence rate in the data insertion process is improved. Our current analyses, with focus on PV, are certainly in agreement with their results.

4.2.3 Analysis of mixed data insertion

The analysis of the case of mixed data insertion is discussed here. Figure 15 (a) presents the most unstable wavenumber one for the case of $T_{pv} = 6$ hours and $T_\phi = 6$, 12 and 24 hours along with the case of PV data only for comparison. Stability is achieved for wavenumber one now with $T_\phi = 6$ or 12 hours. Even with $T_\phi = 24$ hours, the spurious growth of wavenumber one is substantially reduced. The linear analysis which agrees with the numerical results qualitatively, though it tends to overestimate the spurious growth of the longest waves. We have found that the limit for T_ϕ to insure a stable behavior of the longest waves increases as T_{pv} increases, consistent with the linear analysis.

4.2.4 Analysis of PV data insertion with divergence penalty

In Figure 15 (b), we show the same PV data insertion case as in Fugre 15 (a) but with a divergence penalty represented by $T_{div} = 6$, 12 and 24 hours. Clearly, instability is reduced to various extents. For $T_{div} = 6$ hours, full stability is gained but the wave is somewhat damped. It is also found (results not shown) that the critical T_{div} to insure stability increases as T_{pv} increases. So divergence penalty may also serve as a viable tool to control the spurious growth of the longest waves if it so occurs.

The linear analysis, again, confirms the stabilizing effect of the divergence penalty as in the numerical results, though it tends to over-estimate the spurious growth.

4.3 Zero PV perturbation of gravity-inertia waves

It has been noticed for some time that the fast (gravity) modes have zero linearized PV from the normal mode point of view (see e.g., Temperton 1988). This was reiterated during the derivation of the slow equations (Lynch 1989). It is also evident from our Eq.(23) that on an f−plane, the PV perturbation vanishes. The implication of this property in our problem is significant: the PV data insertion does not project onto the gravity-inertia waves and only projects onto the slow manifold. In other words, inserting PV data does not excite spurious model gravity-inertia waves. This is certainly a desirable property as Daley and Puri (1980) argued for in an assimilation system.

5 Assimilating TOMS Total Ozone

In this section we describe an assimilation sequence in which total ozone data from the Nimbus 7 TOMS instrument were used as proxy for PV observations. PV is known to be well correlated with ozone mixing ratio at individual levels near the tropopause in the extratropics. Based on a study of pattern correlation coefficients A93 furthermore showed that total ozone C_{TOVS} as calculated from the TOVS ozone channel and assimilated with

a barotropic transport model driven by ECMWF 6-hour forecast winds can be reasonably well reproduced by a PV-based estimator $\tilde{C}$ defined as

$$\tilde{C} = C_0 + \lambda \int_{p_t}^{p_s} PV(p)dp \tag{33}$$

in the northern hemisphere. Eq. (33) states that the total ozone column is determined by a rescaled partial PV column integral plus a background term C_0 to within an error $\epsilon \equiv C_{TOVS} - \tilde{C}$ that is of the same magnitude as the TOVS total ozone retrieval error. C_0 and λ are slowly varying functions of the seasons, while the error term is a random variable with mean zero. The fact that ϵ is comparable to the instrument retrieval error is taken as evidence of the fact that the ozone mixing ratio and the PV are proportional in the height region that contribute to the variability in total ozone. To within the quasi-constant offset given by C_0 the total ozone must therefore be proportional to the pressure-weighted average PV of that region. A93 empirically found the highest correlation between $\tilde{C}$ and C_{TOVS} when p_t was set to 400 hPa, and p_s to 50 hPa.

Riishøjgaard et al. (1996; henceforth R96) examined the validity of eq. (33) in further detail using total ozone from TOMS and GEOS-DAS analysis PV. They found pattern correlation coefficients very similar to those of A92, however, based on a time series analysis they showed that the agreement in the tropics may be largely fortuitous, and that only in the middle and subpolar latitudes does eq. (33) reflect a truly geophysical relationship. They also found marked differences between the northern and southern hemispheres, with the northern hemisphere winter and spring showing by far the best correlation.

In spite of the caveats given above we nevertheless take the combined results of A93 and R96 as justification for assimilating real total ozone measurements from TOMS globally as proxy observations of vertically averaged PV. From the point of view of the assimilation system the interesting aspect of these experiments is not so much the degree of meteorological realism that can be achieved. This will in any case be limited by the fact that the shallow water equations are used to constrain the system. The key point is rather the question of whether a PV assimilation system can actually digest such highly imperfect observations and generate internally consistent geopotential and PV fields from them.

In order to transform the total ozone observations into PV pseudo-observations the background contribution C_0 from eq. (33) was first subtracted from them. The residual $C_{TOMS} - C_0$ was then multiplied by an empirical scaling factor in order for the range of the observations to correspond to the expected range of model PV. Note that although the background contribution C_0 could be extracted from the statistical study of A93 this approach could not be used for the scaling factor (λ in eq. 33), since the actual values of shallow water PV are different from those of vertically averaged primitive equation model PV.

The TOMS instrument was flying in a polar near sun-synchroneous orbit, and observations were taken near local noon at a resolution of roughly 50 by 50 km at the nadir point. The observations thus cover the globe outside of the polar night region once every 24 hours, but

for every observation time as defined in the assimilation system there is only data available over a small part of the globe, while the rest is unobserved. The observation slots are 30 minutes, corresponding to data insertion in every timestep. All data obtained within a $\pm 15min$ cut-off with respect to a given observation time are thus taken as valid at that time, and for each model grid cell a simple mean of all valid measurements within the cell is defined to be the observation.

The model is run from an initial state of rest with a basic height of 12km. Ozone data are inserted whenever available. In order to separate the temporal range of influence of an observation from the choice of timestep used in the model integration, we insert any given observation gradually during a 6-hour window. For a given model time t_m observations outside the interval $(t_m - 3h; t_m + 3h)$ is not used. Inside that interval the observations are weighted with a cosine bell curve that has its maximum at t_m and then being inserted into the model. The nudging coefficient used corresponds to an e-folding time of 24 hours.

We now show results from an assimilation run beginning on February 5, 1992, 0 Z. After an initial spin-up period the flow gradually develops into a mature pattern after 5 days and it subsequently keeps evolving with the inserted total ozone data.

PV, geopotential, and divergence after 10 days of integration (verified on Feb.15, 1992) are presented in Figure 16 (a-c). For comparision aggregate TOMS total ozone data resampled to the model resolution for the 24 hours from February 15, 00 Z through February 16, 00 Z is shown in Figure 17. The model PV matches the observed total ozone field relatively well in the northern hemisphere. The vortex that corresponds to the high PV region is well produced. Even the poleward intrusion of the equatorial air over the central-west Pacific in the northern hemisphere is captured. The geopotential field produced is very consistent with the PV field, and it does have a certain amount of meteorological credibility. As was to be expected from the results of R96 the link between the dynamical fields of Figure 16 and the ozone field of Figure 17 is strongest in the northern hemisphere.

One thing worth noting is that even though we are inserting patches of proxy PV data that are very unevenly distributed in time and space, the flow fields that are reconstructed from these data are actually mainly large-scale. This is also true for the divergence field (Figure 16(c)). We attribute this to the fact that PV data insertion only projects onto the slow manifold. Even very noisy data distributed in a highly inhomogeneous way thus seem to lead to fields that need little in the way of filtering in order to control unwanted gravity waves.

6 Conclusions and Discussions

The notice of the high correlation between a tracer field such as ozone and the PV field indicates possible availability of proxy PV data. It has been known that PV is a dynamically significant quantity through which many other quantities can be derived if certain balance conditions are assumed. In other words, PV can be regarded as a "master" quantity in a dynamical system. From the data assimilation point of view, PV contains information

13

of both the mass field and the wind field and thus has much to offer. But this may also be a problem. The model is then required to dynamically adjust quickly enough in order to partition the inserted PV information between the wind field and the mass field in a consistent manner. How would a model respond?

We have made an initial attempt to address this issue. The shallow water PV-D model and a simple nudging algorithm were used. A model simulated polar vortex was used as the testbed. The results are very encouraging and point to the potential power PV data may offer in a data assimilation system. The linear analyses, which agree reasonably well with the numerical experiments, gave us some more insight. We can summarize our results as follows: 1) The primitive shallow water model recovers the full dynamical fields with PV data being inserted if an appropriate nudging coefficient is chosen; 2) Both the numerical experiments and the linear analysis indicate that there is little scale-dependency of convergence for the case of PV data insertion, but there is strong scale-dependency for the case of the geopotential data insertion; 3) PV data insertion does not excite spurious gravity-inertia waves for PV projects only onto the slow manifold. Gravity-inertia waves have zero PV perturbation; 4) The model absorbs the TOMS total ozone observations as proxy PV data very well. The constructed geopotential field and divergence field are coherent and dynamically consistent.

The above results all together lead us to conclude that tracer observations, as proxy PV data, may offer potential power in a data assimilation system. Though the data insertion algorithm used in this study is very simple, the results are very encouraging.

Acknowledgments

References

Allaart, M. A. F., H. Kelder and L. C. Heijboer, 1993: On the relation between ozone and potential vorticity. *Geophys. Res. Lett.*, **20**, 811-814.

Anthes, R. A., 1974: Data assimilation and initialization of hurricane prediction models. *J. Atmos. Sci.*, **31**, 702-719.

Bates, J. R., Y. Li, A. Brandt, S. F. McCormick and J. Ruge, 1995: A global shallow-water numerical model based on the semi-Lagrangian advection of potential vorticity. *Q. J. R. Meteorol. Soc.*, **121**, 1981-2005.

Bates, J. R. and Y. Li, 1996: Simulation of stratospheric vortex erosion using three different global shallow water numerical models. *In :Numerical methods for atmospheric and oceanic modelling, Andre J. Robert memorial volume of Atmosphere-Ocean).*

Charney, J., M. Halem and R. Jastrow, 1969: Use of incomplete historical data to infer the present state of the atmosphere. *J. Atmos. Sci.*, **26**, 1160-1163.

Daley, R., 1995: Estimating the wind field from chemical constituent observations: Experiments with a one-dimensional extended Kalman filter. *Mon. Wea. Rev.*, **123**, 181-198.

Daley, R. and K. Puri, 1980: Four-dimensional data assimilation and the slow manifold. *Mon. Wea. Rev.*, **108**, 85-99.

Danielsen, E. F., 1968: Stratospheric-tropospheric exchange based on radioactivity, ozone and potential vorticity. *J. Atmos. Sci.*, **25**, 502-518.

Davies, H. C. and R. E. Turner, 1977: Updating prediction models by dynamical relaxation: an examination of the technique. *Q. J. R. Meteorol. Soc.*, **103**, 225-245.

Douglass, A. R., R. B. Rood, R. S. Stolarski, M. R. Schoeberl, M. H. Proffitt, J. J. Margitan, M. Loewenstein, J. R. Podolske, S. E. Strahan, 1990: Global three-dimensional constituent fields derived from profile data. *Geophys. Res. Lett.*, **17**, (4), 525-528.

Hoskins, B. J., M. E. McIntyre and A. W. Robertson, 1985: On the use and significance of isentropic potential vorticity maps. *Q. J. R. Meteorol. Soc.*, **111**, 877-946.

Juckes, M. N. and M. E. McIntyre, 1987: A high-resolution one-layer model of breaking planetary waves in the stratosphere. *Nature*, **328**, 590-596.

Kistler, R. and R. McPherson, 1975: On the use of a local wind correction technique in four-dimensional data assimilation. *Mon. Wea. Rev.*, **103**, 445-449.

Kuo, Y.-H., Y.-R. Guo, E. R. Westwater, 1993: Assimilation of precipitable water measurements into a mesoscale numerical model. *Mon. Wea. Rev.*, **121**, 1215-1238.

Lait, L. R., M. R. Schoeberl, P. A. Newman, M. H. Proffitt, M. Loewenstein, J. R. Podolske. S. E. Strahan, K. R. Chan, B. Gary, J. J. Margitan, E. Browell, M. P. McCormick and A. Torres, 1990: Global three-dimensional constituent fields derived from profile data. *Geophys. Res. Lett.*, **17**, 525-529.

Li, Y. and J. R. Bates, 1996: A study of the behaviour of semi-Lagrangian models in the presence of orography. *Q. J. R. Meteorol. Soc.*, **122**, 1675-1700.

Lynch, P., 1989: The slow equations. *Q. J. R. Meteorol. Soc.*, **115**, 201-219.

Mariotti, A., B. Legras and D. G. Dritschel, 1994: Vortex stripping and the erosion of coherent structures in two-dimensional flows. *Phys. Fluids*, **6**, 3954-3962.

Norton, W., 1994: Breaking Rossby waves in a model stratosphere diagnosed by a vortex-following coordinate system and a technique for advecting material contours. *J. Atmos. Sci.*, **51**, 654-673.

Polvani, L. M., D. W. Waugh and R. A. Plumb, 1995: On the subtropical edge of the stratospheric surf zone. *J. Atmos. Sci.*, **52**, 1288-1309.

Riishøjgaard, L. P., 1996: On four-dimensional variational assimilation of ozone data in weather prediction models. *Q. J. R. Meteorol. Soc.*, **122**, 1545-1572.

Riishøjgaard, L. P. and E. Källén, 1996: On the correlation between ozone and potential vorticity for large-scale Rossby waves. *J. Geophys. Res.*,**Accepted**.

Riishøjgaard, L. P., G.-P. Lou, R. Ménard, and S. E. Cohn, A study of the correlation between TOMS total ozone and GEOS-DAS PV during February 1992. *(Manuscript submitted to the Proceedings of the XVIII Quadrennial Ozone Symposium, Sept. 1996)*.

Ruge, J., Y. Li, S. F. McCormick, A. Brandt and J. R. Bates, 1996: A nonlinear multigrid solver for a global numerical shallow water model based on the semi-Lagrangian advection of potential vorticity. *SIAM J. Sci. Comput.*, **in press**.

Temperton, C., 1988: Implicit normal mode initialization. *Mon. Wea. Rev.*, **116**, 1013-1031.

Vallis, G. K., 1996: Potential vorticity inversion and balanced equations of motion for rotating and stratified flows. *Q. J. R. Meteorol. Soc.*, **122**, 291-322.

Williamson, D. and A. Kasahara, 1971: Adaptation of meteorological variables forced by updating. *J. Atmos. Sci.*, **28**, 1313-1324.
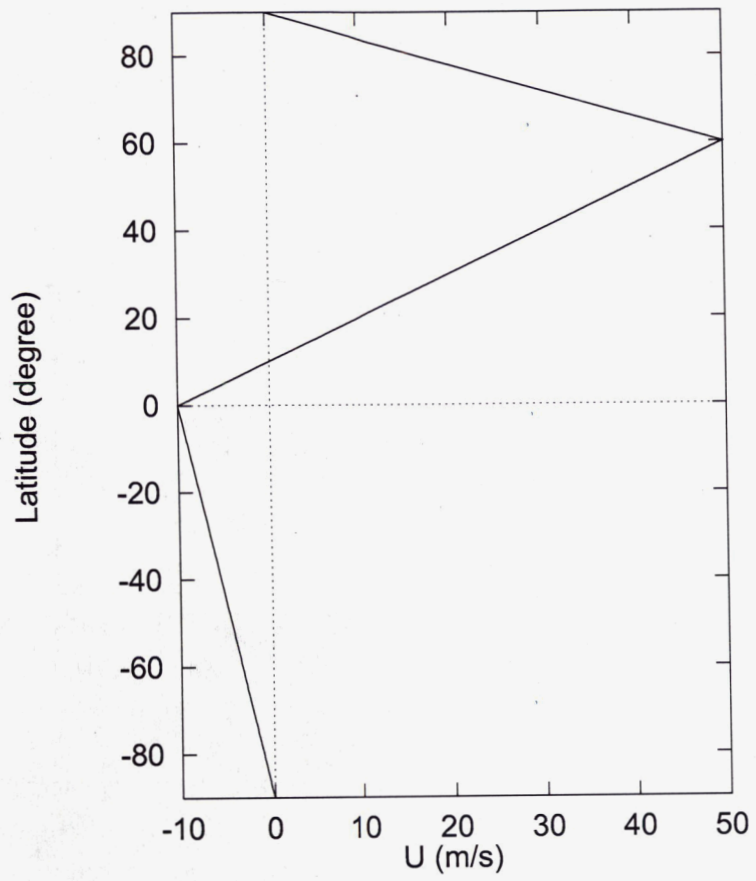
Figure 1: Initial zonal wind (m/s).
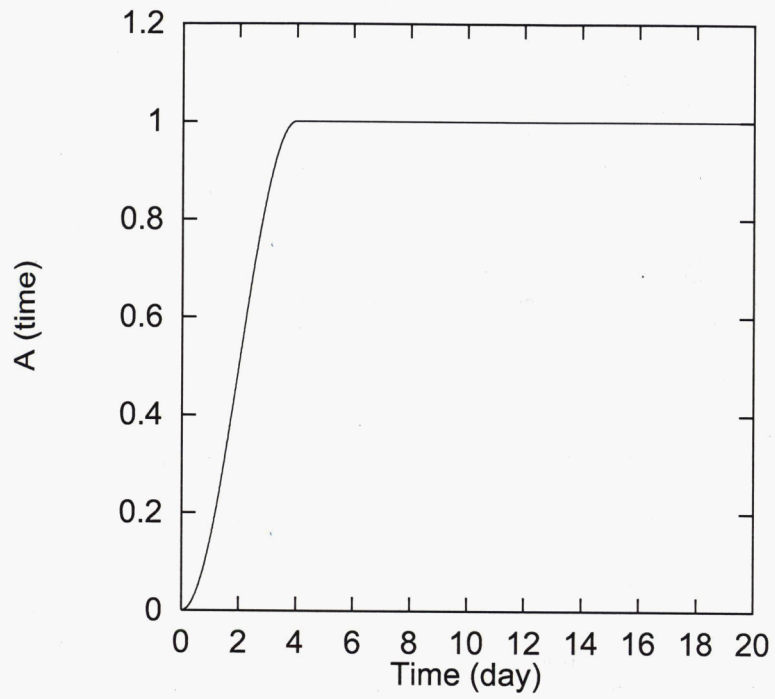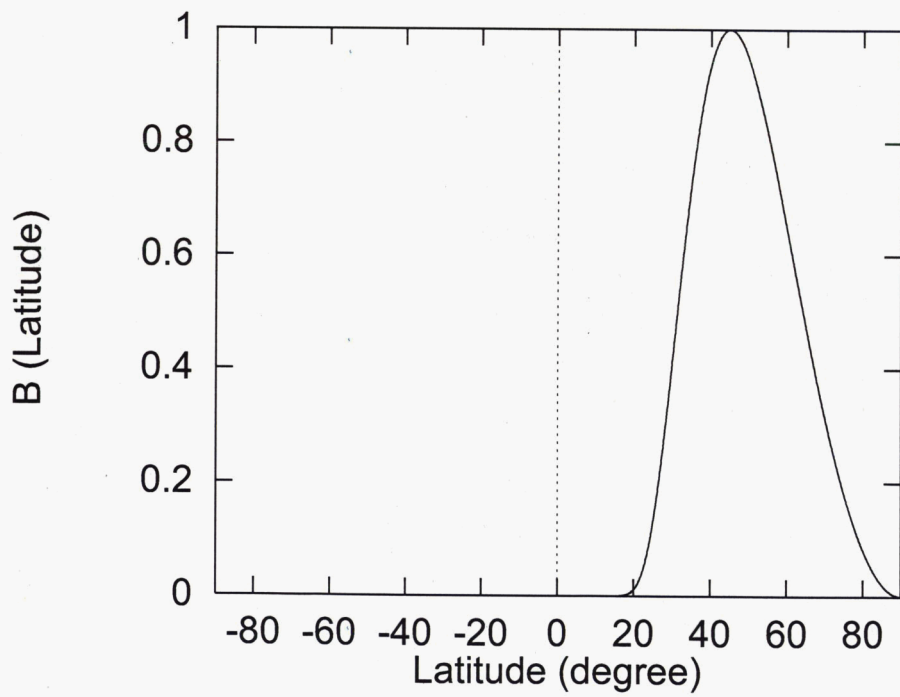
Figure 2: Functions used to specify the orographic forcing. (a) $A(t)$; (b) $B(\phi)$.
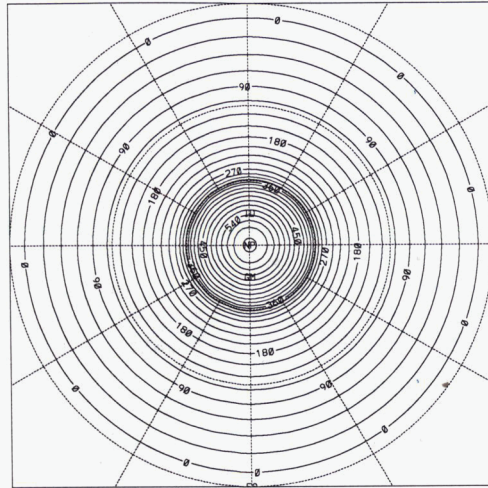
CONTOUR FROM 0.00000E+00 TO 0.60750E-08 CONTOUR INTERVAL OF 0.22500E-09 PT(3,3)= 0.93056E-10 LABELS SCALED BY 0.10000E+12
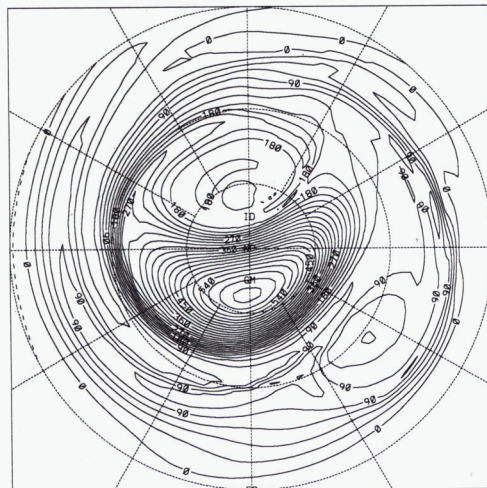
(a)

CONTOUR FROM -0.22500E-09 TO 0.60750E-08 CONTOUR INTERVAL OF 0.22500E-09 PT(3,3)= 0.12697E-09 LABELS SCALED BY 0.10000E+12
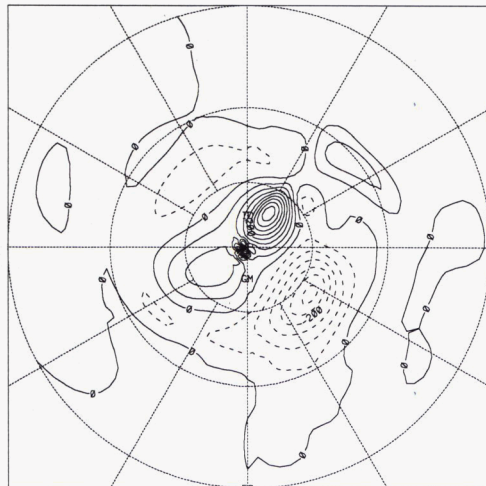
(b)

Fig 3 (to be continued)
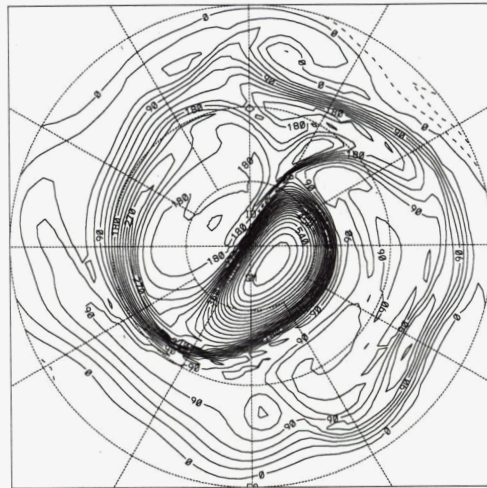
CONTOUR FROM -0.45000E-09 TO 0.60750E-09 CONTOUR INTERVAL OF 0.22500E-09 PT(3,3)= 0.17100E-09 LABELS SCALED BY 0.10000E+12

(c)
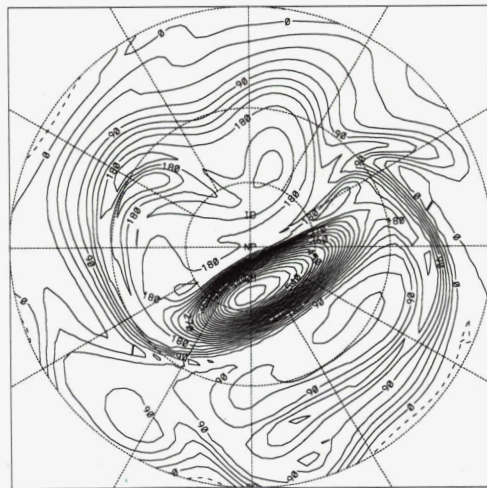
CONTOUR FROM -0.22500E-09 TO 0.63000E-09 CONTOUR INTERVAL OF 0.22500E-09 PT(3,3)= 0.10072E-09 LABELS SCALED BY 0.10000E+12

(d)

Figure 3: PV evolution of the control, i.e., the "data". (a) Day 0; (b) Day 20; (c) Day 30; (d) Day 50. Contour interval = 22.5 (in $10^{-11}m^{-2}s$).
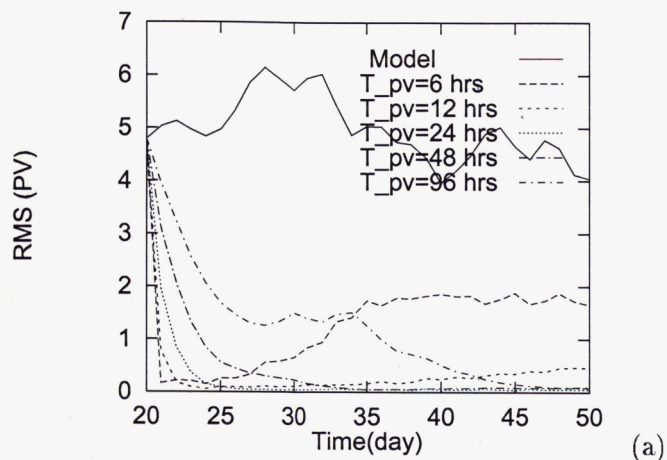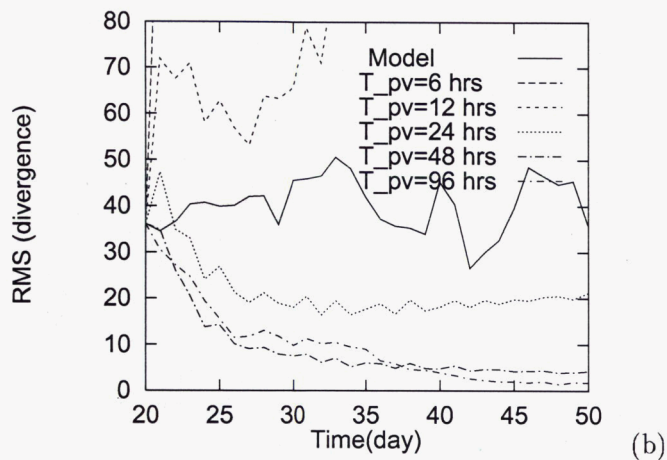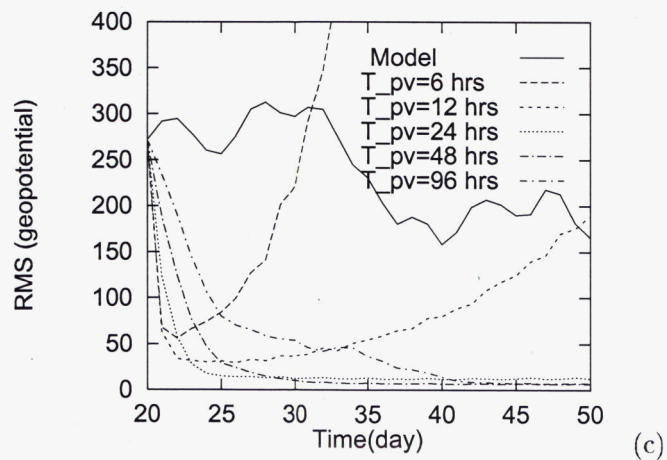
Figure 4: RMS errors for the experiments of PV data insertion with various lengths of e-folding time. (a) PV ($10^{-10}m^{-2}s$); (b) Divergence ($10^{-8}s^{-1}$); (c) Geopotential (m).
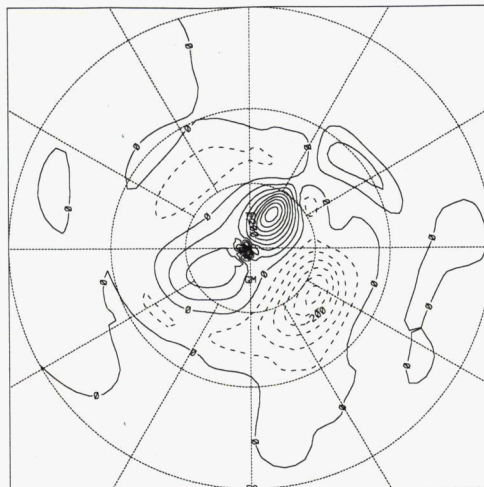
CONTOUR FROM -0.30000E-05 TO 0.40000E-05 CONTOUR INTERVAL OF 0.50000E-06 PT(3,3)= -0.11354E-06 LABELS SCALED BY 0.10000E+09

(a)
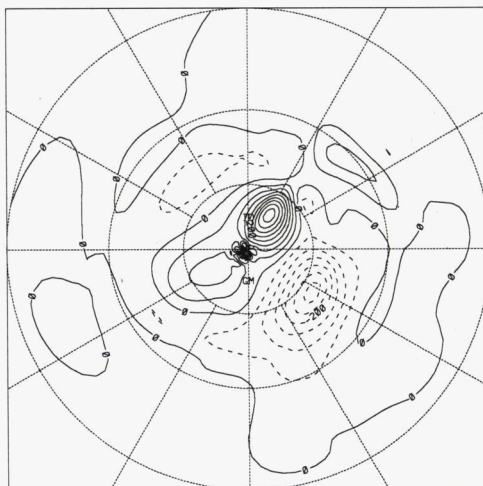
CONTOUR FROM -0.30000E-05 TO 0.40000E-05 CONTOUR INTERVAL OF 0.50000E-06 PT(3,3)= -0.14054E-07 LABELS SCALED BY 0.10000E+09

(b)

Fig 5 (to be continued)

CONTOUR FROM -0.12000E-04 TO 0.75000E-05 CONTOUR INTERVAL OF 0.50000E-06 PT(3,3)= -0.29511E-07 LABELS SCALED BY 0.10000E+08
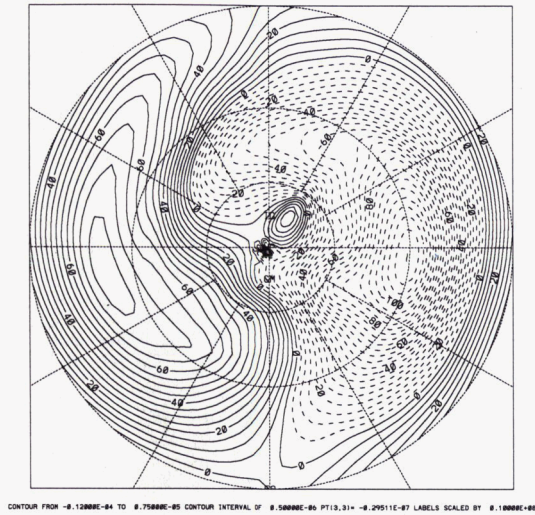
(c)

Figure 5: Divergence at Day 30. Contour interval $= 50.0$ $(10^{-8}s^{-1})$. (a) the control; (b) the assimilated with $T_{pv} = 48$ hours; (c) the assimilated with $T_{pv} = 6$ hours.
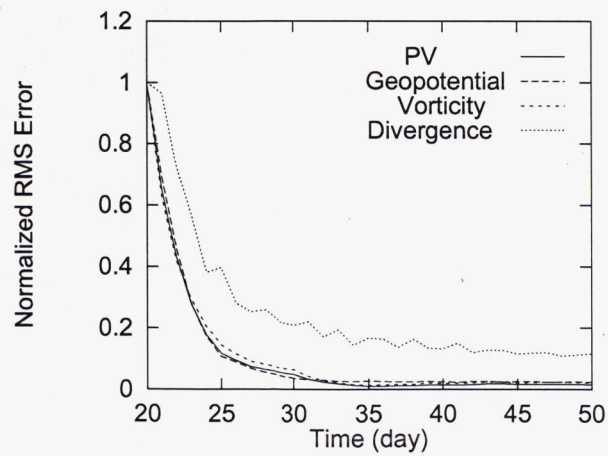
Figure 6: Normalized RMS errors for the case of PV insertion with $T_{pv} = 48$ hours.

23
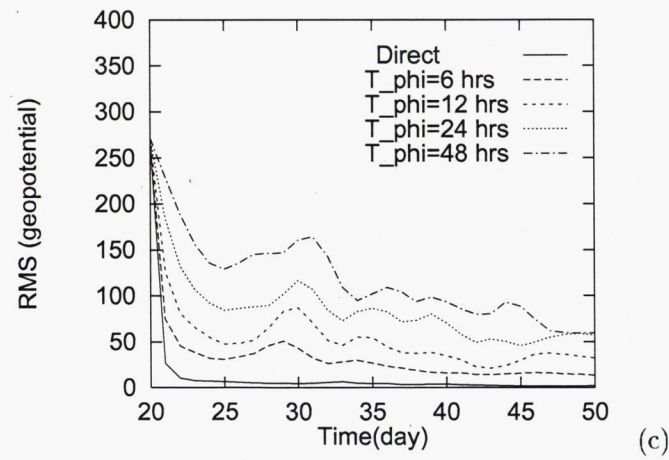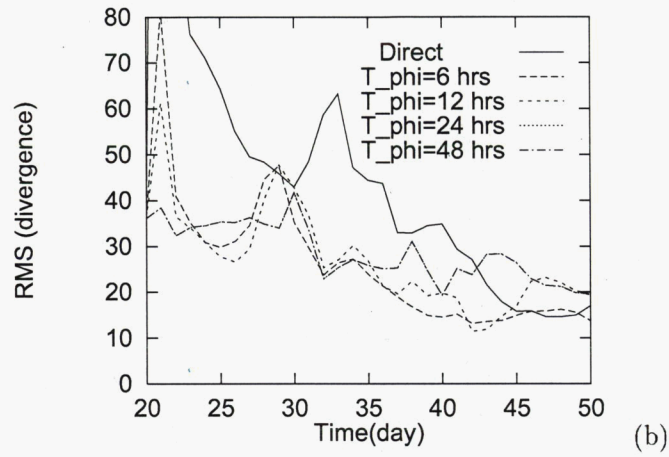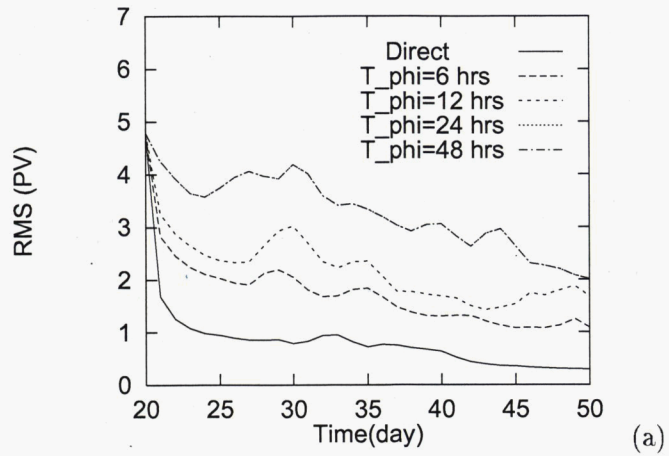
Figure 7: RMS errors for the cases of geopotential data insertion: (a) PV ($10^{-10}m^{-2}s$); (b) Divergence ($10^{-8}s^{-1}$); (c) Geopotential height(m)
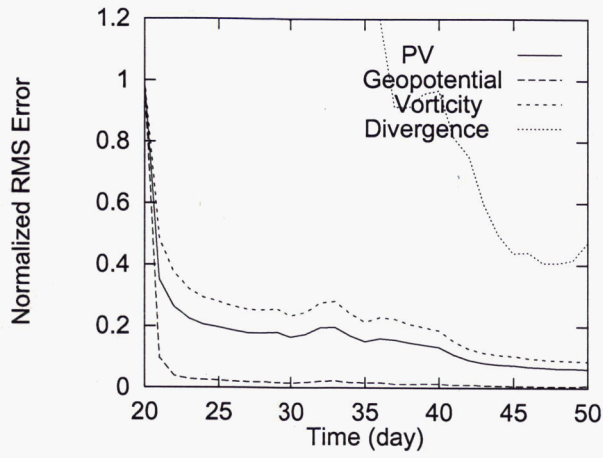
Figure 8: Normalized RMS errors for the case of direct insertion of geopotential data.
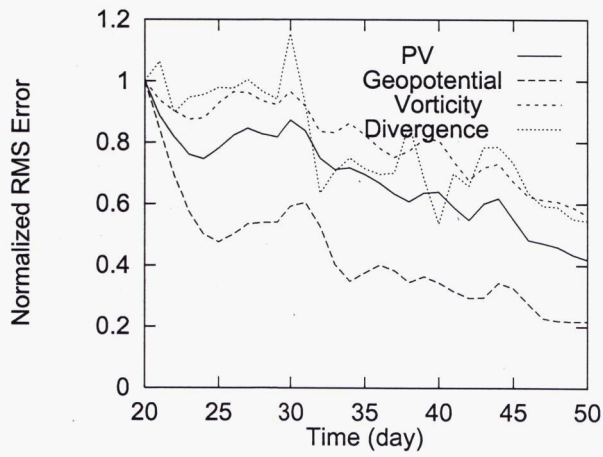
Figure 9: Normalized RMS errors for the case of geopotential data insertion with $T_\phi = 48$ hours.
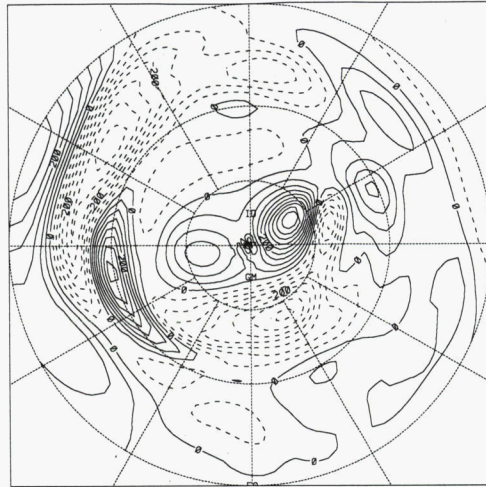
(a)
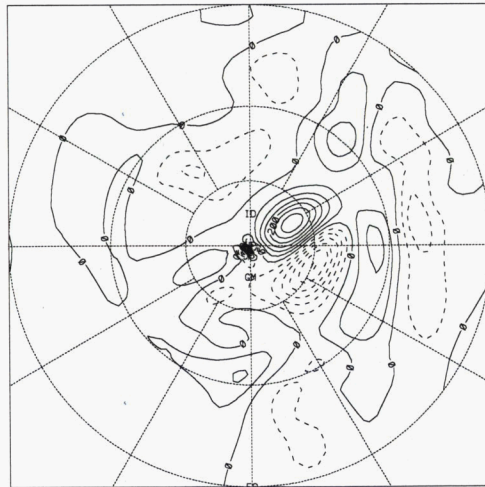
(b)

Figure 10: Divergence for the case of direct geopotential insertion. Contour interval $= 50.0$ $(10^{-8}s^{-1})$. (a) Day 24; (b) Day 50.
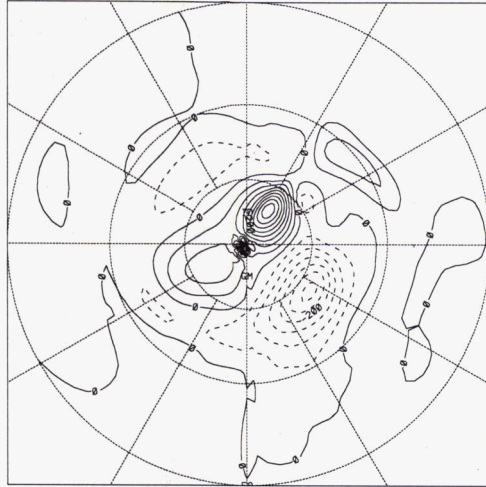
CONTOUR FROM -0.30000E-05 TO 0.40000E-05 CONTOUR INTERVAL OF 0.50000E-06 PT(3,3)= -0.14567E-08 LABELS SCALED BY 0.10000E+09

(a)

CONTOUR FROM -0.30000E-05 TO 0.40000E-05 CONTOUR INTERVAL OF 0.50000E-06 PT(3,3)= 0.21294E-08 LABELS SCALED BY 0.10000E+09

(b)

Fig 11 (to be continued)

CONTOUR FROM -0.30000E-05 TO 0.40000E-05 CONTOUR INTERVAL OF 0.50000E-06 PT(3,3)= 0.50578E-07 LABELS SCALED BY 0.10000E+09
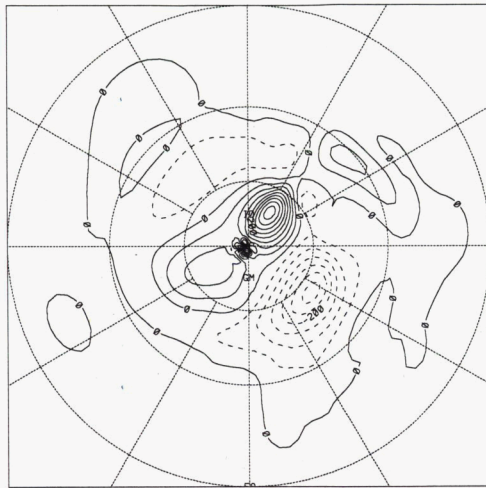
(c)

Figure 11: Divergence at Day 30 for the case of mixed data insertion with $T_{pv} = 6$ hours and (a) $T_\phi = 6$ hours; (b) $T_\phi = 12$ hours; (c) $T_\phi = 24$ hours. Contour interval = 50.0 $(10^{-8}s^{-1})$.
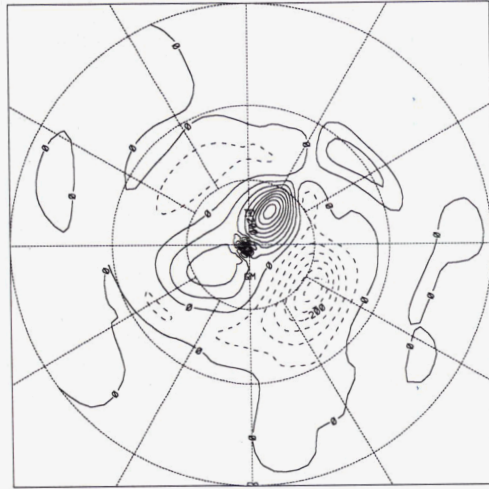
CONTOUR FROM -0.30000E-05 TO 0.40000E-05 CONTOUR INTERVAL OF 0.50000E-06 PT(3,3)= -0.16736E-07 LABELS SCALED BY 0.10000E+09

(a)
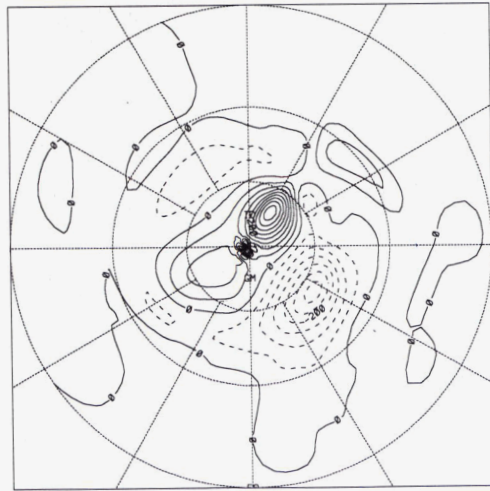
CONTOUR FROM -0.30000E-05 TO 0.40000E-05 CONTOUR INTERVAL OF 0.50000E-06 PT(3,3)= -0.14163E-07 LABELS SCALED BY 0.10000E+09

(b)

Fig 12 (to be continued)
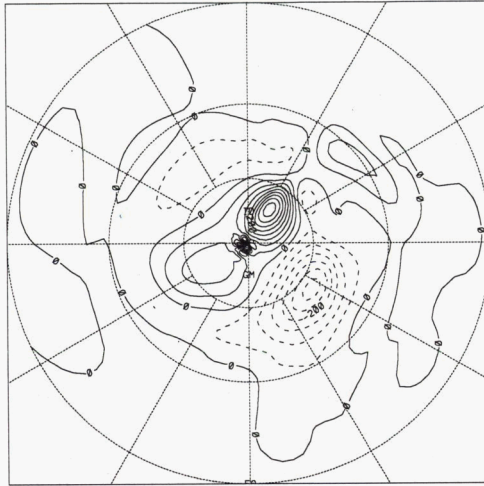
29

(c)

Figure 12: Divergence at Day 30 for the case of PV data insertion ($T_{pv} = 6$ hours) with a divergence penalty: (a) $T_\phi = 6$ hours; (b) $T_\phi = 12$ hours (c) $T_\phi = 24$ hours. Contour interval $= 50.0$ $(10^{-8}s^{-1})$.
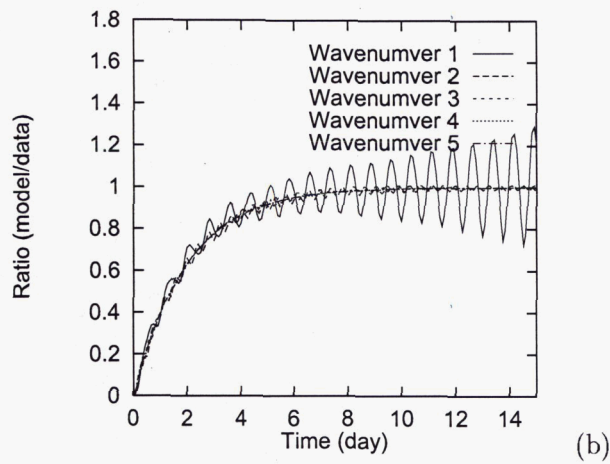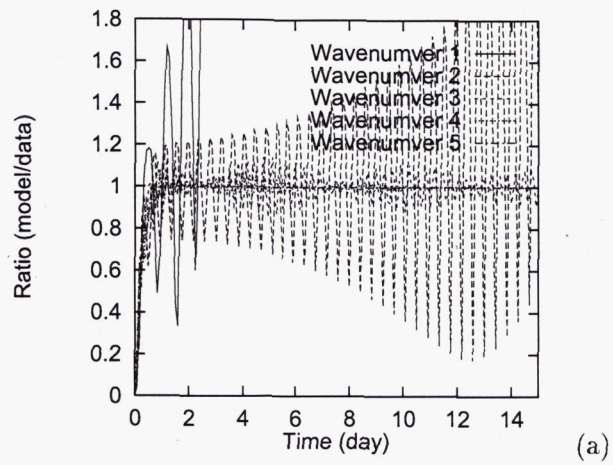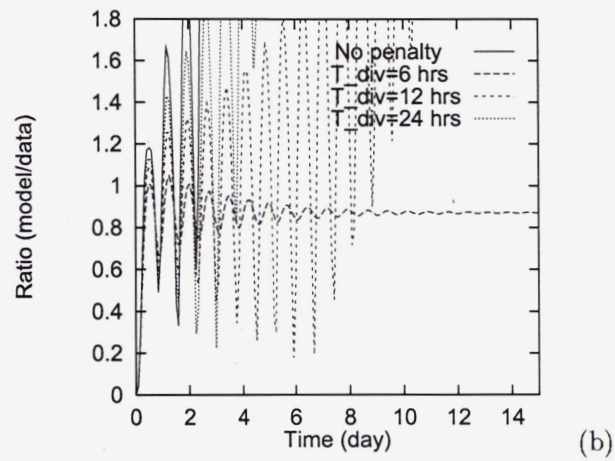
Figure 13: Ratio of the amplitudes of the linear solutions to those of the data for the case of PV data insertion with (a) $T_{pv} = 6$ hours; (b) $T_{pv} = 48$ hours.
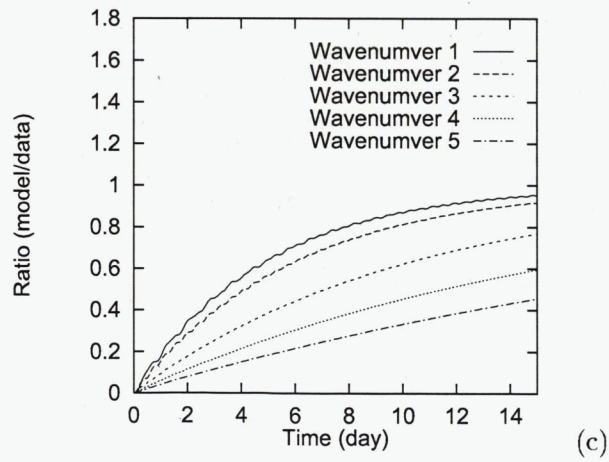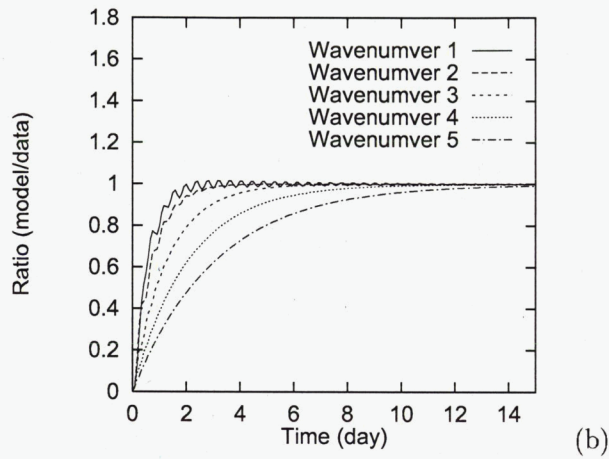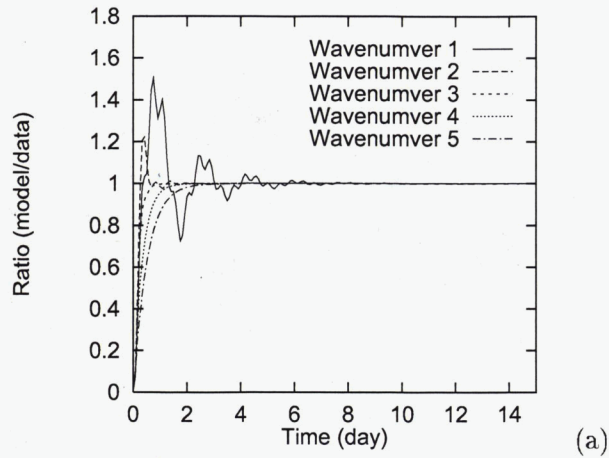
Figure 14: Ratio of the linear solution to the data for the case of geopotential data insertion with (a) $T_\phi = 1$ hour; (b) $T_\phi = 6$ hours; (c) $T_\phi = 48$ hours
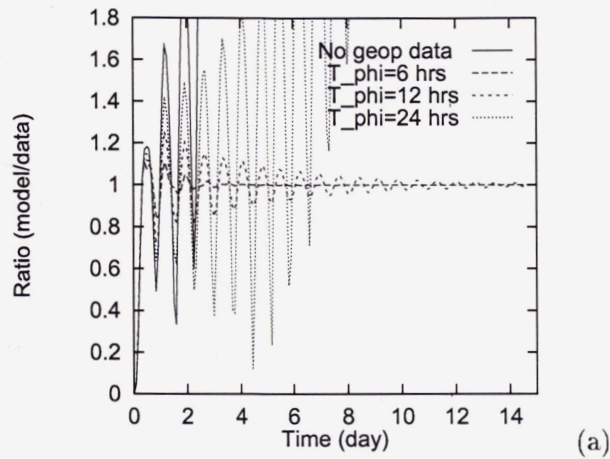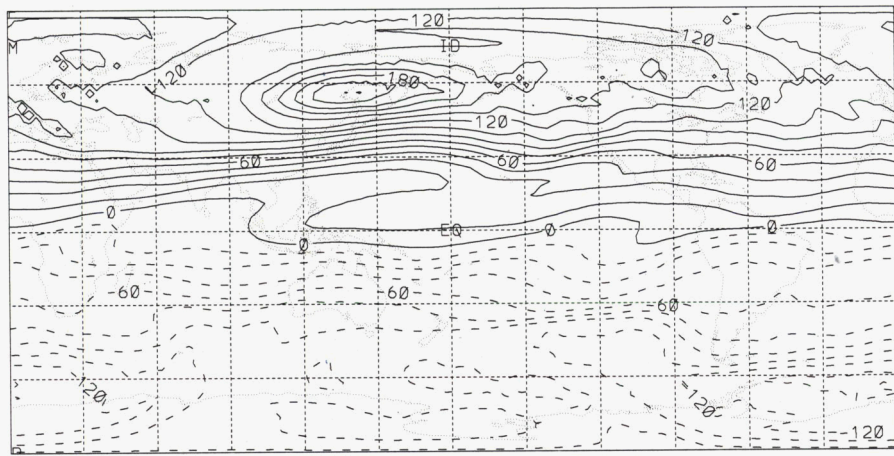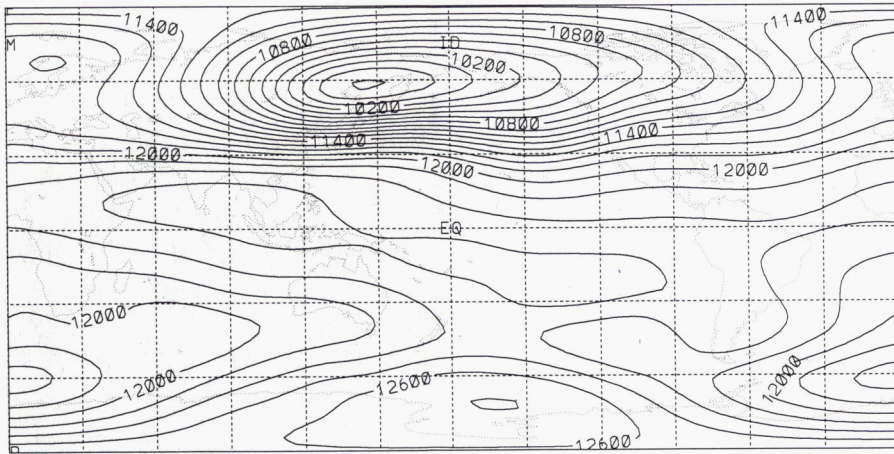
Figure 15: Ratio of the amplitudes of the linear solution to those of the data for wavenumber one. (a) Mixed data insertion ($T_{pv} = 6$ hours); (a) PV data insertion ($T_{pv} = 6$ hours) with divergence penalty.

CONTOUR FROM -0.13500E-08 TO 0.21000E-08 CONTOUR INTERVAL OF 0.15000E-09 PT(3,3)= -0.11323E-08 LABELS SCALED BY 0.10000E+12
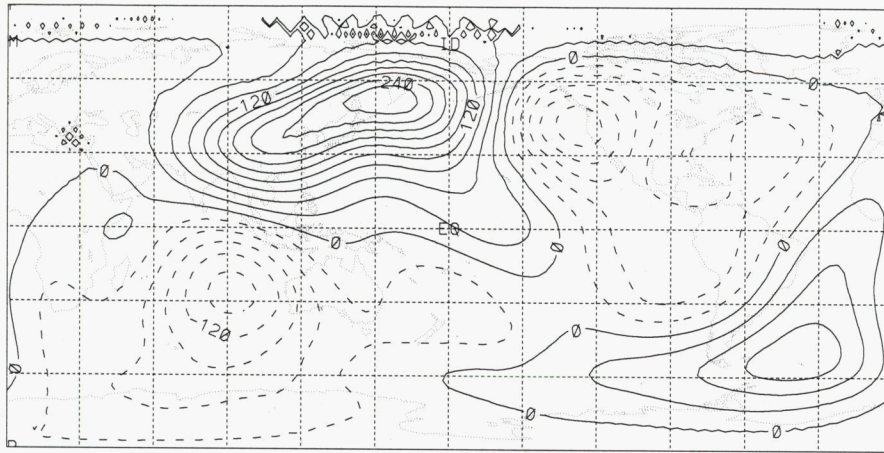
(a)

Fig 16 (to be continued)

CONTOUR FROM   9600.0   TO   12750.   CONTOUR INTERVAL OF   150.00   PT(3,3)=   12358.

(b)

Fig 16 (to be continued)

CONTOUR FROM -0.15000E-05 TO 0.27000E-05 CONTOUR INTERVAL OF 0.30000E-06 PT(3,3)= -0.28074E-06 LABELS SCALED BY 0.10000E+09

(c)

Figure 16: Model fields of Day 10 (verified on Feb.15, 1992) from the integration of assimilating the TOMS total ozone data. (a) PV (contour interval=$15.0 \times 10^{-11} \, m^{-2}s$); (b) Geopotential height (contour interval=$150.0 \, meters$); (c) Divergence (contour interval=$30.0 \times 10^{-8}s^{-1}$).
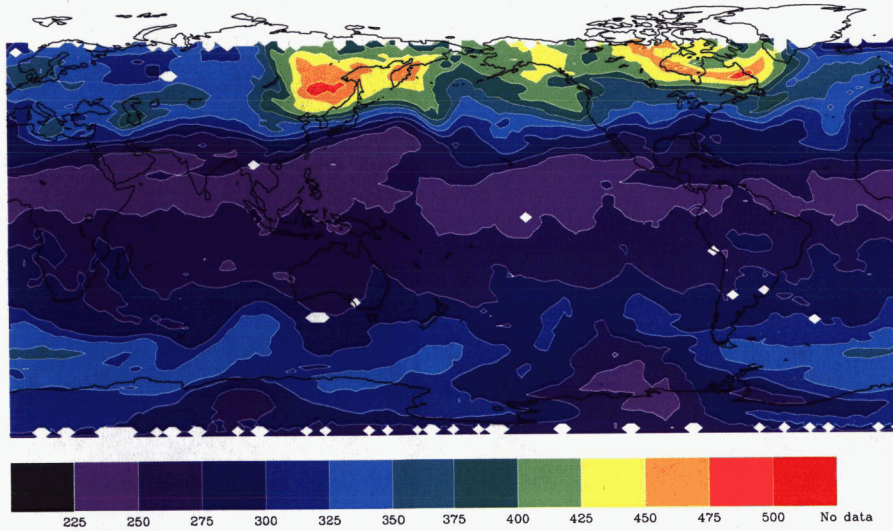
TOMS total ozone, Feb 15, 1992

Figure 17: TOMS total ozone on Feb.15, 1992.